Tampere University

Tuomas Pihlava

EPSILON-NEAR-ZERO MEDIATED LONG-RANGE FÖRSTER RESONANCE ENERGY TRANSFER PROCESS

Faculty of Engineering and Natural Sciences
Bachelor of Science Thesis
Examiners: Assoc. Prof. Humeyra Caglayan
Dr. Alireza Rahimi Rashed
May 2020

ABSTRACT

Tuomas Pihlava: Epsilon-near-zero mediated long-range Förster resonance energy transfer process
Bachelor of Science Thesis
Tampere University
Degree Programme in Engineering and Natural Sciences
May 2020

Optical metamaterials consisting of unit cells much smaller than the wavelengths of incident light can be used to precisely engineer light-matter interactions. Metamaterials composed of alternating dielectric and metal layers can be used to achieve extraordinary properties, such as propagating high-k waves and epsilon-near-zero (ENZ) behaviour on a certain range of wavelengths.

Förster resonance energy transfer (FRET) is a mechanism of energy transfer between two fluorescent molecules. Typically, FRET takes place when the molecules are separated by no more than 10 nm. However, it has been proposed that a multi-layer nanostructure can be used to achieve over tenfold increase of this range. Furthermore, the physical background of this phenomenon is predominantly unknown. In this thesis, multi-layer nanostructures are studied as a means of mediating FRET over distances much longer than usual Förster distances.

The thesis is divided into two parts. The first part, as the literature review part, concentrates on the properties, fabrication, and applications of multi-layer nanostructures and how they can be used to achieve hyperbolic and ENZ behaviour in a material. Furthermore, a review of photoluminescence and FRET processes is provided. Finally, crucial spectroscopy methods utilized in the experimental part are reviewed.

In the experimental part, the FRET process is studied between two organic dye molecules, Coumarin 485 and LDS 798. The experiments were conducted by steady-state and time-resolved fluorescence spectroscopy measurements. The results demonstrated energy transfer occurring between these molecules. In addition, three multi-layer nanostructures compatible with the mentioned dye molecules were designed based on the introduced theory. The first structure displays dielectric behaviour on the spectral range where FRET takes place. The second structure is an ENZ material and the third one shows hyperbolic behaviour on that range. The results provided in this thesis can be used to conduct a more thorough investigation of FRET mediated by multi-layer nanostructures displaying different optical properties.

Keywords: hyperbolic metamaterials, multi-layer metamaterials, epsilon-near-zero, ENZ metamaterials, Förster resonance energy transfer

The originality of this thesis has been checked using the Turnitin OriginalityCheck service.

CONTENTS

LIST OF FIGURES

LIST OF SYMBOLS AND ABBREVIATIONS

Ag	Silver
Al	Aluminium
Al_2O_3	Aluminium oxide
AOTF	Acoustic optical tunable filter
Au	Gold
BG	Background
C 485	Coumarin 485
CdSe	Cadmium selenide
CdTe	Cadmium telluride
E-beam	Electron-beam
ENZ	Epsilon-near-zero
FDTD	Finite-difference time-domain
FRET	Förster resonance energy transfer
HMM	Hyperbolic metamaterial
MBE	Molecular beam epitaxy
NA	Numerical aperture
OTT	Optical topological transition
PDOS	Photonic density of states
PECVD	Plasma-enhanced chemical vapor deposition
PL	Photoluminescence
PMMA	Polymethyl methacrylate
PMMA A4	4% of PMMA and 96% of anisole
QD	Quantum dot
RIE	Reactive ion etching
rpm	Revolutions per minute
S	Singlet state
SiO_2	Silicon dioxide
SPAD	Single-photon avalanche diode
T	Triplet state

Ta_2O_5	Tantalum pentoxide
TCSPC	Time-correlated single photon counting
TDC	Time to digital converter
TEM	Transverse electromagnetic
TiO_2	Titanium dioxide
TMM	Transfer-matrix method
UV	Ultraviolet
WD	Working distance
ZnS	Zinc sulfide

a	unit cell size
Abs	absorbance
α_i	intensity of a lifetime component
c	speed of light
$\vec{D}$	electric displacement
$\vec{E}$	electric field
d_d	thickness of dielectric layers
d_m	thickness of metal layers
E	energy
ϵ	permittivity
ϵ_A	extinction coefficient of acceptor
E_{FRET}	Förster resonance energy transfer efficiency
f	frequency
h	The Planck constant
I	intensity
$J(\lambda)$	spectral overlap integral
k	wavevector
κ^2	dipole orientation factor
k_{FRET}	Förster resonance energy transfer rate
k_{nr}	nonradiative decay rate
k_r	radiative decay rate
λ	wavelength
m	mass
M	molar mass

μ	permeability
n	refractive index
ω	angular frequency
Φ	quantum yield
$\parallel$	parallel component
$\perp$	perpendicular component
ρ	metal fill fraction
r	separation distance
R_0	Förster distance
Ref	reflectance
τ	lifetime
t	time
Tra	transmittance
v_p	phase velocity
$wt\%$	weight ratio concentration

1 INTRODUCTION

Optical metamaterials are artificial structures that consist of elements much smaller than the wavelengths of light. This allows them to have unique properties not found elsewhere in nature, such as negative refraction [1], subwavelength imaging [2, 3] and epsilon and mu near zero [4, 5]. Metamaterials allow precise engineering of light-matter interaction, and thus have been a topic of extensive research in the recent years.

Hyperbolic metamaterials (HMMs) are one example of artificial nanostructures. These structures have been shown to possess unique properties regarding their isofrequency surfaces, allowing high-k waves to propagate, as opposed to regular dielectric media. Another important feature of HMMs is the increased photonic density of states. [6] These structures are easy to fabricate and have already proven to be good candidates for many applications. The isofrequency properties of an HMM are dependent on wavelength, and proper engineering allows the shape of the isofrequency surface to be either elliptical or hyperbolic in a given spectral region. In addition, the effective permittivity of the materials goes to zero for certain wavelengths, thus called epsilon near zero (ENZ) wavelengths. In these wavelengths, completely different physical phenomena such as waves propagating long distances with negligible phase variation, take place [4].

Another important phenomenon covered in this thesis is Förster resonance energy transfer (FRET) process , originally discovered by Theodor Förster. FRET is a radiationless energy transfer process between two light-sensitive emitters [7]. However, FRET is highly sensitive to distance between the pair, which hinders its usability in many applications.

The ENZ region of an HMM has previously been shown to mediate FRET over an increased distance between CdSe/ZnS quantum dots and Cy3 fluorescent dye molecule [8]. In this thesis, I explore how FRET between two organic dye molecules is affected by a sub-wavelength metal and dielectric multi-layer structure. The study is expanded to compare how the three different regimes of an HMM affect the energy transfer process, with a special interest on the transfer through an ENZ-medium. This demonstrates coupling of donor and acceptor over distances much longer than normally possible. Research to understand the possibilities of metamaterials to mediate nonradiative interactions is vital for development of many promising applications such as quantum entanglement [9] and increasing the efficiency of several nanodevices [10].

Chapter 2 provides information of sub-wavelength structures that are used to realize ENZ and hyperbolic metamaterials. In chapter 3, photoluminescence (PL) phenomena and

FRET process are introduced. Chapter 4 introduces the methods used to acquire the results of this thesis, while the achieved results are presented in chapter 5. In chapter 6, the thesis is concluded and an outlook to future work is provided.

2 HYPERBOLIC METAMATERIALS

Research on the field of metamaterials aims to engineer the response of a material to electromagnetic waves. This is achieved using artificial materials consisting of structures much smaller than the wavelengths of the incident light. Hyperbolic metamaterials (HMMs) are one of the most promising materials for many practical applications [3, 11].

The interaction between a medium and an incident electric field is determined by the permittivity tensor of the material which is given by

$$\epsilon = \begin{bmatrix} \epsilon_{xx} & 0 & 0 \\ 0 & \epsilon_{yy} & 0 \\ 0 & 0 & \epsilon_{zz} \end{bmatrix}, \tag{2.1}$$

where ϵ_{xx}, ϵ_{yy} and ϵ_{zz} are the permittivities in respective directions [12]. For conventional dielectric media and vacuum the permittivity is same in each direction. These kind of materials are called isotropic. The dispersion relation of such media is

$$k_x^2 + k_y^2 + k_z^2 = \frac{\omega^2}{c^2}, \tag{2.2}$$

where $k = [k_x, k_y, k_z]$ is the wavevector, ω is the angular frequency of the wave and c is the speed of light. For a single frequency ω both sides of the equation are constant. In this case, the equation depicts a surface of wavevectors where the frequency stays constant, called an isofrequency surface. For isotropic media, the shape of this surface is a sphere [2, 3, 11, 13].

A hyperbolic metamaterial is a structure of extreme anisotropy, specially a uniaxial crystal. The permittivity of such uniaxial medium is the same in the two directions that are perpendicular with respect to the plane of incidence ($\epsilon_{xx} = \epsilon_{yy} = \epsilon_{\parallel}$). The permittivity is different in the third direction, parallel to the plane of incidence($\epsilon_{zz} = \epsilon_{\perp}$). For such material, the dispersion relation of extraordinary (Transverse Magnetic) waves is expressed as

$$\frac{k_x^2 + k_y^2}{\epsilon_{\parallel}} + \frac{k_z^2}{\epsilon_{\perp}} = \frac{\omega^2}{c^2}, \tag{2.3}$$

which distorts to an ellipsoid instead of sphere of the isotropic case. However, in the case of an extreme anisotropy the two components have different signs $\epsilon_{\parallel} > 0$ and $\epsilon_{\perp} < 0$ or $\epsilon_{\parallel} < 0$ and $\epsilon_{\perp} > 0$. In either case the isofrequency surface opens up and forms a

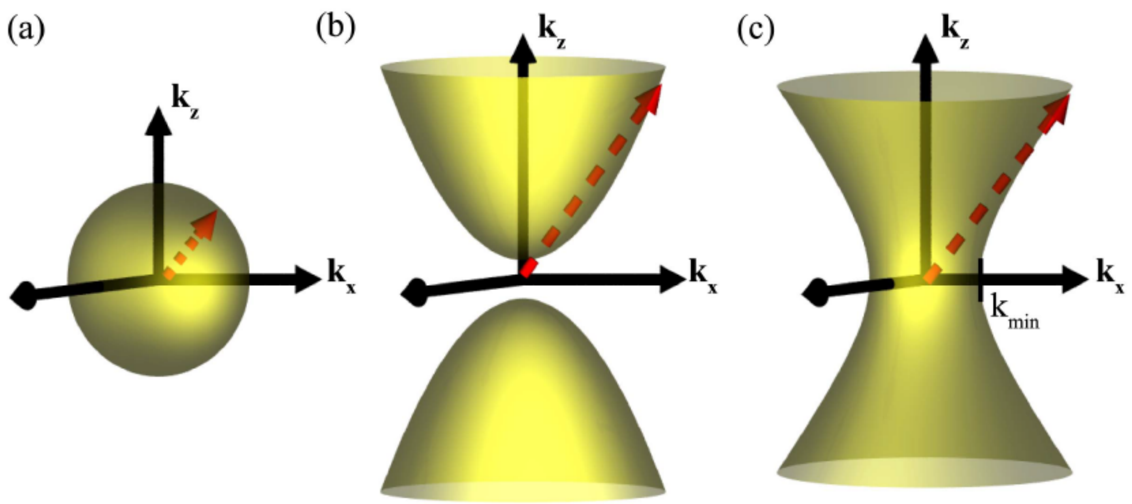

Figure 2.1. *k-space topology. (a) For a conventional isotropic dielectric the isofrequency surface is a sphere. Only waves with limited k-vectors are supported. (b) For a metamaterial with one negative component of the permittivity tensor ($\epsilon_{\|} > 0$ and $\epsilon_{\perp} < 0$, Type I HMM) the isofrequency surface is a double-sheeted hyperboloid. Both low-k and high-k waves are supported. (c) For a metamaterial with two negative components of the permittivity tensor ($\epsilon_{\|} < 0$ and $\epsilon_{\perp} > 0$, Type II HMM), the isofrequency surface is a single-sheeted hyperboloid. Waves with parallel wavevectors above k_{min} are supported, and below k_{min} are reflected. The red arrows represent the wavevectors supported by the material. [13]*

hyperbolic shape, hence the term hyperbolic metamaterial is used. [2, 3, 11, 13]

HMMs can be divided to two types. Type I HMM has only one negative component of the permittivity tensor ($\epsilon_{\|} > 0$ and $\epsilon_{\perp} < 0$), while type II HMM has two negative components ($\epsilon_{\|} < 0$ and $\epsilon_{\perp} > 0$). [2, 3, 11, 13]

The isofrequency surface limits the waves that are allowed to propagate in the material. In the regime of hyperbolic dispersion, waves with infinite wavevectors are allowed to propagate in the material. These modes, called the high-k modes, are evanescent in regular media and susceptible to exponential decay. [2, 3, 11, 13] The different isofrequency surfaces in k-space are shown in Figure 2.1.

Another important property of HMMs is the increased photonic density of states (PDOS). Photonic states, similar to electronic states, describe the amount of states a photon with certain energy is able to occupy in a system. According to Fermi's golden rule, spontaneous emission from quantum emitters depends on PDOS. This leads to the number of radiative decay channels being directly proportional to PDOS. Thus, increased PDOS can be experimentally studied by probing radiative decay lifetimes of emitters in the vicinity of the metamaterial. These lifetimes will be drastically shortened when PDOS increases. [6, 14]

An intuitive description is that PDOS is the volume constrained between two isofrequency contours $\omega(k)$ and $\omega(k) + \Delta\omega$. As the volume between two hyperboloids diverges to infinity, an infinite PDOS in the hyperbolic regime is predicted by this analysis. [2, 3, 6, 11, 13] More formal definition and mathematical examination for increased PDOS in an HMM can be achieved using formalism based on dyadic Green's function [13, 15].

Theoretical examination predicts both propagating modes with infinite k-vectors and infinite PDOS. However, the allowed high-k modes and PDOS predicted by this examination have some practical limitations. All realistic designs used to achieve hyperbolic behavior in a material require the use of metals. By nature, metals always introduce optical losses to the system. Thus, all realistic HMMs absorb a portion of the waves propagating through them, reducing the portion of transmitted waves.

Another limitation is the size of the unit cell. Unit cell is defined as the smallest fully symmetric unit that is repeating over the structure. The effective medium theory only remains valid while the size of the unit cell is much smaller than the wavelength of the incident light. Actual structures only support effective wavevectors up to the inverse of the unit cell size a, such that $k_{eff} \sim 1/a$. These waves lie at the edge of the Brillouin zone. Waves with larger wavevectors are not transmitted since they perceive the sructure as a photonic crystal instead of a metamaterial. They are affected by Bragg scattering instead. [2, 13]

2.1 Fabrication

In metals, the real part of the permittivity tensor is negative below the plasma frequency in each of the three directions. This is a consequence of the polarization response of free-electrons in metals. The free-electrons naturally move to the opposite direction than the electric field of the incident wave. [11]

To obtain hyperbolic behaviour, some components of the permittivity tensor need to remain positive. Thus, the motions of free-electrons needs to be restricted in one to two directions. [11] The most common ways to achieve this in visible spectral range are structures of alternating nanolayers of metal and dielectric (Type II HMM) and structures of metallic nanorods embedded in a dielectric host matrix (Type I HMM) [2, 3, 11, 13]. These structures are visualized in Figure 2.2. Other possible realizations include highly magnetized plasma and arrays of metal-dielectric nanopyramids [11].

To fabricate a multi-layer HMM, multiple thin layers of metal and dielectric need to be deposited on top of each other. Most common metals used for applications in the visible region are silver and gold, which can be deposited along an appropriate dielectric using electron beam evaporation. Other methods of fabricating nanolayers include plasma enhanced chemical vapor deposition (PECVD), reactive sputtering, pulsed laser deposition and for III-V semiconductors, molecular beam epitaxy (MBE) . [3]

Fabrication of nanorod HMMs is typically done by electrochemical deposition of silver or gold on a nanoporous dielectric membrane. The dielectric membrane typically consists of alumina and the porosity is achieved by anodization. [3, 11]

This thesis focuses on multi-layer HMMs. These will be fabricated in a cleanroom using

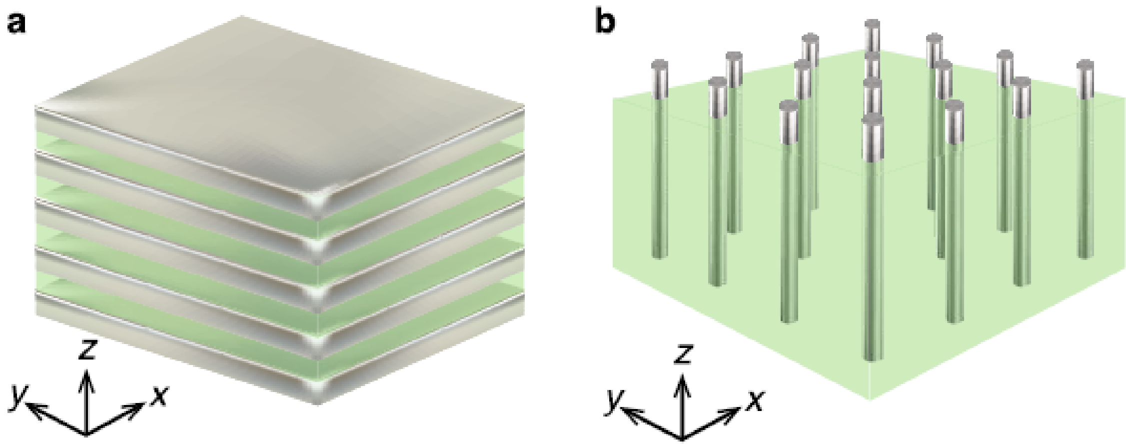

Figure 2.2. *Most common practical realizations of HMMs are (a) multi-layer structures consisting of consecutive metal and dielectric nanolayers and (b) metallic nanorod arrays in a dielectric host matrix. [2]*

electron beam evaporators to produce the multi-layers. The fabrications methods relevant for this thesis are covered in section 4.2.

2.2 Parallel and Perpendicular Permittivities

Effective medium theory provides a way to express the effective parallel and perpendicular permittivities for both multi-layer and nanorod HMM structures when the permittivities of each used material are known. This is crucial for designing a structure showing desired behaviour on chosen wavelengths. This theory predicts that the extreme anisotropy required for an HMM can be achieved both with multi-layer and with nanorod designs. Hyperbolic behaviour is achieved either by changing layer thicknesses of a multi-layer structure or changing the portion occupied by nanorods in the host matrix.

To derive the permittivities, metal fill fraction ρ needs to be defined as

$$\rho = \frac{d_m}{d_m + d_d}, \tag{2.4}$$

where d_m and d_d are the total summed thicknesses of metal and dielectric layers.

First, effective parallel permittivity is derived. From the definition of permittivity it is known that

$$\vec{D} = \vec{\epsilon}_{eff}\vec{E}, \tag{2.5}$$

where $\vec{D}$ is the electric displacement in the medium caused by an electric field $\vec{E}$ and $\vec{\epsilon}_{eff}$ is the effective permittivity of the medium. The tangential component of the electric field remains continuous across an interface, thus

$$E_m^{\parallel} = E_d^{\parallel} = E^{\parallel}, \tag{2.6}$$

where $E_m^{\parallel}$, $E_d^{\parallel}$ and $E^{\parallel}$ are the parallel component of the electric field in metal layers, dielectric layers and the metamaterial. The overall electric displacement across the material is found by averaging the contributions of both metal and dielectric layers:

$$D^{\|} = \rho D_m^{\|} + (1-\rho) D_d^{\|}, \tag{2.7}$$

where $D_m^{\|}$, $D_d^{\|}$ and $D^{\|}$ are the displacements in metal layers, dielectric layers and the metamaterial.

Combining equations 2.5, 2.6 and 2.7 the effective parallel permittivity of the metamaterial is found to be

$$\epsilon_{\|} = \rho\epsilon_m + (1-\rho)\epsilon_d. \tag{2.8}$$

Next, the effective perpendicular permittivity will be derived. At an interface, the normal component of the electric displacement vector stays constant

$$D_m^{\perp} = D_d^{\perp} = D^{\perp}, \tag{2.9}$$

where $D_m^{\perp}, D_d^{\perp}$ and $D^{\perp}$ are the electric displacement in the metal layers, the dielectric layers and the metamaterial. Based on the superposition principle, the total electric field in the metamaterial is the sum of the field components in the metal and dielectric layers such that

$$E^{\perp} = \rho E_m^{\perp} + (1-\rho) E_d^{\perp}, \tag{2.10}$$

where $E_m^{\perp}$, $E_d^{\perp}$ and $E^{\perp}$ are the perpendicular components of the electric field in metal layers, dielectric layers and the metamaterial. Combining equations 2.5, 2.9 and 2.10 the effective perpendicular permittivity of the metamaterial is discovered to be

$$\epsilon_{\perp} = \frac{\epsilon_m \epsilon_d}{\rho\epsilon_d + (1-\rho)\epsilon_m}. \tag{2.11}$$

Similar derivation based on effective medium theory could be applied for the HMM structure based on metal nanorods in a dielectric host. This scrutiny gives the parallel permittivity as

$$\epsilon_{\|} = \rho\epsilon_m + (1-\rho)\epsilon_d \tag{2.12}$$

and the perpendicular permittivity as

$$\epsilon_{\perp} = \frac{(1+\rho)\epsilon_m\epsilon_d + (1-\rho)\epsilon_d^2}{(1-\rho)\epsilon_m + (1+\rho)\epsilon_d} \tag{2.13}$$

for a nanorod HMM [3, 13].

The incident electromagnetic waves perceive a different permittivity in a material based on their wavelength. This is related to a phenomenon called dispersion. Due to this effect, the calculated effective permittivities are different for each wavelength of incident radia-

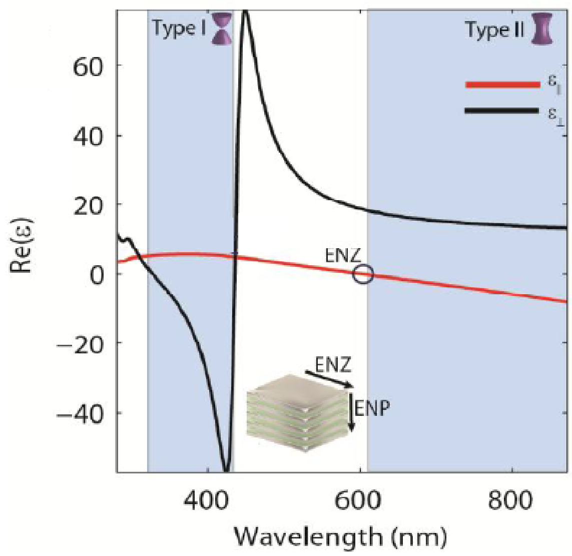

Figure 2.3. *Parallel and perpendicular permittivities for a multi-layer structure predicted by effective medium theory. The structure consists of alternating layers of Ag and TiO_2 using 35% silver fill fraction. $\epsilon_{\|}$ and $\epsilon_{\perp}$ are calculated using equations 2.8 and 2.11. Elliptical regime is depicted as white and hyperbolic regime as blue. The ENZ point between the regimes is also highlighted. Adapted from reference [3].*

tion. Figure 2.3 shows the varying of effective permittivities over different wavelengths calculated for a multi-layer HMM.

Based on the signs of different component of the permittivity tensor, an HMM has three regimes, which appear at different wavelengths. Elliptical regime ($\epsilon_{\|} \cdot \epsilon_{\perp} > 0$) shows behavior similar to a conventional dielectric, while the hyperbolic regime ($\epsilon_{\|} \cdot \epsilon_{\perp} < 0$) is the regime of the extraordinary properties such as propagating high-k waves and increased PDOS. The Epsilon-Near-Zero (ENZ) regime is the spectral region where $\epsilon_{\|}$ goes through zero for a multi-layer HMM and $\epsilon_{\perp}$ goes through zero for a nanorod HMM. In this regime, some unique physical properties can be observed. These properties are extensively examined in section 2.4. Equations 2.8 and 2.11 can be used to detect the location of each regime in the spectrum.

2.3 Reflectance and Transmittance Properties

Reflectance and transmittance are defined as the proportions of light that are reflected and transmitted by the material, respectively. Typically metals are highly reflective, while dielectrics are mostly transparent. For multi-layer HMMs, characteristic behaviour of both dielectrics and metals can be observed on different wavelengths. On lower wavelengths the HMM will show transmittance values of a typical dielectric, while on higher wavelengths it shows high reflectance. Furthermore, the transition from highly transparent to highly reflective behaviour has been observed to take place at the same spectral region where the ENZ-point is located. This relations applies to multi-layer HMMs specifically. [16, 17]

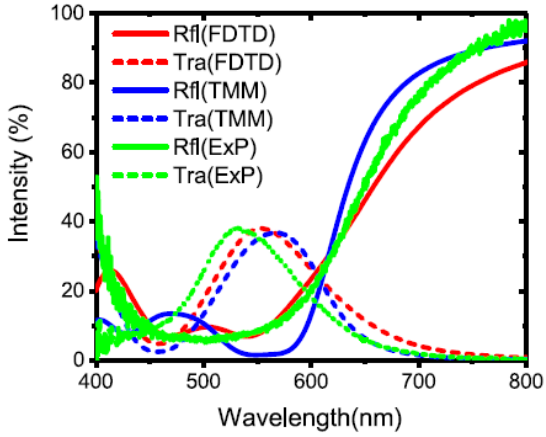

Figure 2.4. *Transmittance (Tra) and reflectance (Rfl) values of a multi-layer HMM consisting of layers of 15.5nm Au and 37.5 nm* TiO_2*. The graph shows the values acquired using Finite-difference time-domain (FDTD) simulations, Transfer-matrix method (TMM) and experimental measurements. The transition from transparent to reflective behaviour happens near the ENZ-wavelengths (*$\lambda_{ENZ} = 605nm$*). [16].*

There are a few commonly used methods to acquire the reflectance and transmittance of a metamaterial. These include Finite-difference time-domain (FDTD) and Transfer-matrix method (TMM) simulations [16]. Reflectance and transmittance behaviour for a multi-layer HMM structure acquired using these methods is represented in Figure 2.4 along with experimental reflectance and transmittance data.

2.4 ENZ properties

The Epsilon-Near-Zero (ENZ) regime is located in between the elliptical and hyperbolic regimes. In this regime $\epsilon_{||}$ changes sign from positive to negative. In the elliptical regime the isofrequency surface of the material was a closed elliptical surface. The changing sign of $\epsilon_{||}$ causes this surface to open up as a hyperboloid. This is called an optical topological transition (OTT). [18] Opening of the isofrequency surface causes the material to support high-k modes and an infinite PDOS.

Minimal permittivity in this regime gives rise to a number of unique physical phenomena, one being low wavenumber k, leading to nonexistent spatial dispersion. This in turn causes minimal phase variation over long physical distances. The behaviour of the wave is static while propagating inside an ENZ material. Thus, a wave with arbitrary wavefront entering an ENZ interface will leave the ENZ media with a unified wavefront [4]. This effect is illustrated in Figure 2.5 (a).

Another property of an ENZ material is high phase velocity v_p, which is given by equation

$$v_p = \frac{1}{\sqrt{\epsilon\mu}} = f\lambda, \tag{2.14}$$

where ϵ and μ are the permittivity and permeability of the material, f is the frequency

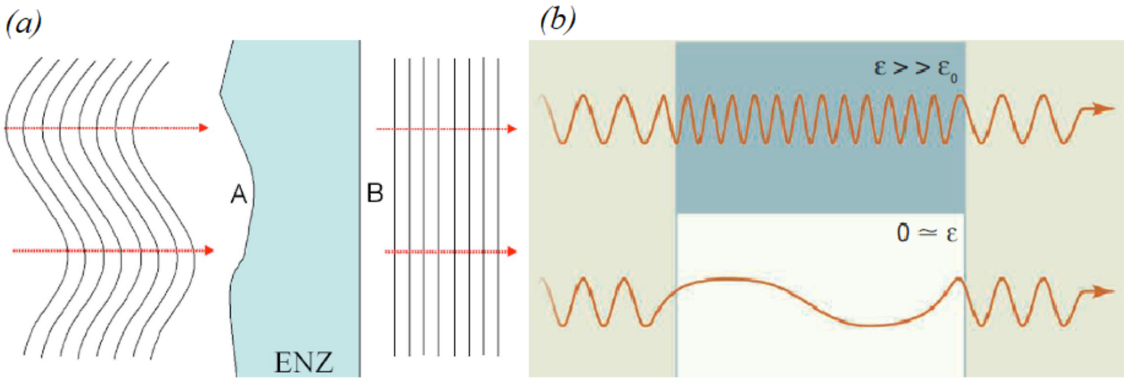

Figure 2.5. *(a) An arbitrary wavefront entering an ENZ interface. Due to small phase variation, the field becomes static inside the material. After the exit interface, the electric field has become a homogeneous plane wave. [4] (b) As a consequence of low wavenumber, waves entering an ENZ medium have their wavelengths "stretched" [19].*

of the wave and λ is the wavelength. In conventional media, waves with high frequencies generally have short wavelengths. As a consequence of high phase velocity, high frequencies and high wavelengths are allowed to exist simultaneously. [19] This effect of stretched wavelength in an ENZ medium is displayed in Figure 2.5 (b).

ENZ materials are interesting from the point of view of geometrical optics as well. Snell's law describes the deflection of light at an interface between two materials. The law is written as

$$n_1 sin\theta_1 = n_2 sin\theta_2, \tag{2.15}$$

where n_1 and n_2 are the refractive indices of both materials, and θ_1 and θ_2 are the angles between the normal of the interface and the incident and refracted waves respectively. For an ENZ material the refractive index is $n = \sqrt{\epsilon\mu} \approx 0$. If the beam is propagating from an ENZ material to another medium such as air, the left side of the equation will be zero. Thus, θ_2 is also forced to be zero and the beam will exit along the normal of the interface independently of angle θ_1. Such behaviour is called directionality and it can be taken advantage of when designing plasmonic nanoantennas. [20]

Similar treatment can be applied when a beam is propagating from a non-zero-index medium to an ENZ medium. Due to right side of equation 2.15 being zero, all waves coming to the interface in angles $\theta_1 \neq 0$ will be subject to total internal reflection. Thus, virtually all light will be reflected. [21]

Field confinement is another property of ENZ materials. Permittivity being zero causes local negative polarizability. Furthermore, boundary conditions in the interface between ENZ and regular media require high normal component of the electric field, leading to field confinement, supporting highly directive leaky waves and field localization. Field confinement leads to the electric field concentrating inside a small region, thus causing field enhancement. [22]

Other unique effects perceived in the ENZ regime include enhanced nonlinear effects

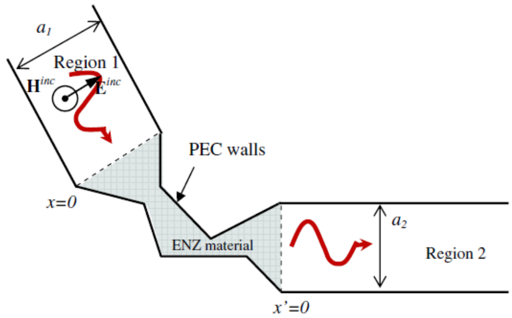

Figure 2.6. *An electromagnetic wave is able to tunnel through an arbitrary shaped ENZ waveguide due to supercoupling. [26]*

[23], small group velocity [24, 25] and supercoupling. The latter allows waves to tunnel through a very narrow ENZ-filled waveguide that can be of any length, shape and orientation [26]. The supercoupling phenomenon is visualized in Figure 2.6.

2.5 Applications

To conclude this chapter, certain applications of HMMs will be briefly discussed to help in achieving a better understanding of their unusual properties. These are sub-wavelength imaging and the hyperlens.

Light scattering from an object contains information of its spatial features. In conventional optics, the used wavelength limits the maximum resolution of the output image due to the diffraction limit. The information of larger features is carried by waves with relatively small wavevectors, while information of sub-wavelength details is carried by the high-k waves. Since the high-k waves do not propagate, the information they contain is lost. However, by bringing an HMM to the near-field of the object these waves are converted to propagating waves inside the material. Therefore, the information of the subwavelength features carries to the output face of the metamaterial. Unfortunately, these waves are evanescent outside the HMM. [2, 3]

The hyperlens is an improvement to fix the aforementioned issue. If an HMM is designed in a cylindrical fashion, the magnitude of wavevectors containing the subwavelength information can be reduced in the material. This enables the propagation of these waves after leaving the material. This phenomenon is explained due to conservation of angular momentum $m \sim k_\theta r = constant$, where k_θ is the tangential component of the momentum and r is the radius from the image point to the point in the material. As the high-k waves propagate through the hyperlens, the radius increases and consequently, the wavevector is compressed. [2, 3]

3 PRINCIPLES OF RESONANCE ENERGY TRANSFER

To understand the resonance energy transfer process, one needs to have the basic understanding of light-matter interactions and the photoluminescence process. In this chapter these concepts are discussed. The Förster Resonance Energy Transfer (FRET) process as well as some spectroscopy methods, which are needed to observe this process, are described.

3.1 Absorption and Photoluminescence Processes

The interaction between a material and a particle is determined based on the energy states in the material. The energy states are quantized, meaning that the energy of the material can get only certain discrete values. These states are divided into rotational, vibrational and electronic states. The electronic states have the highest energy differences between them, and are able to be excited by photons in the ultraviolet and visible spectral regions. Vibrational and rotational energy states have lower energies, and are thus not excitable by photons with high energy. [7]

Photoluminescence is a process where an excited particle emits a photon when it relaxes back to its lowest electronic state, called the ground state. A particle capable of participating in the photoluminescence process is referred as a chromophore. The energy of a photon emitted by a fluorescent particle is given by

$$E_{photon} = \Delta E = E_e - E_0 = hf, \tag{3.1}$$

where E_e is the energy of the excited state, E_0 is the energy of the ground state, E_{photon} is the energy of the photon which is equal to the band gap between the energy states ΔE, h is the Planck constant and f is the frequency of the photon. [7]

Absorption is the reverse process, where a photon whose energy is equal to the energy difference between the ground state and one of the excited states is absorbed by the particle. As a result, the particle moves to the excited state from the ground state. [7]

Jablonski diagrams are an established convention of illustrating processes that occur between the absorption and emission of light. Figure 3.1 shows a typical Jablonski diagram. On top of the diagram are the states with higher energies, while states of lower energy

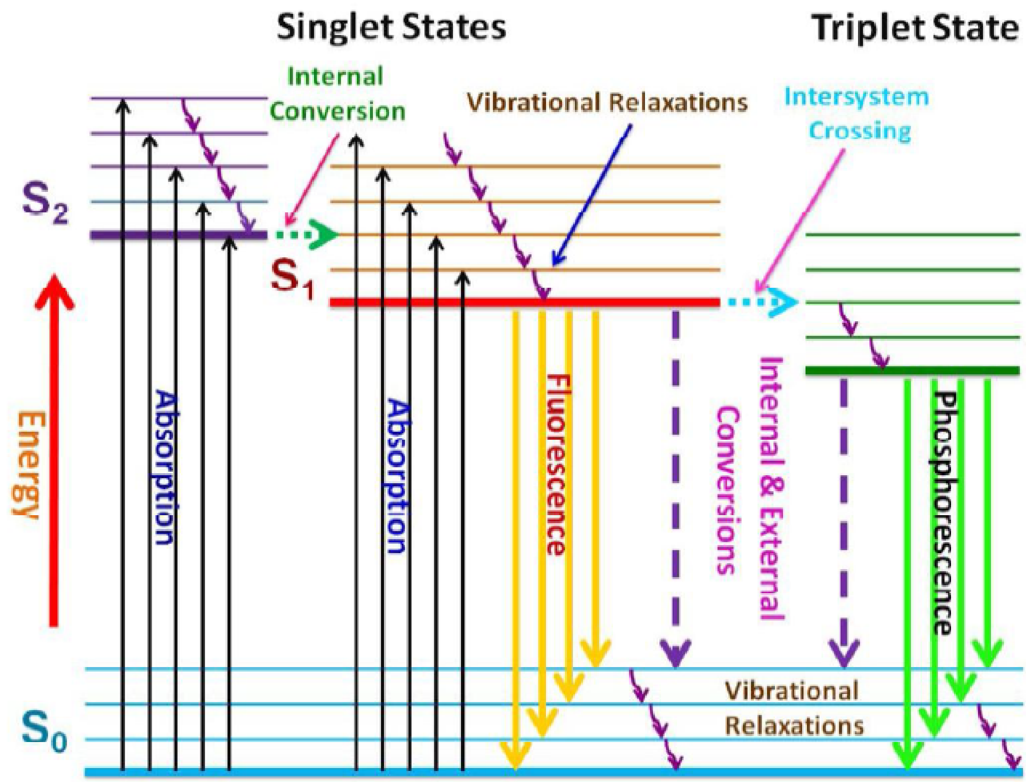

Figure 3.1. *A Jablonski diagram portraying different processes inherent to fluorescent particles. [27]*

are located on the bottom. S_0, S_1 and S_2 depict the ground state and the first and second excited electronic states, respectively. The vibrational energy levels related to each electronic states are shown as thinner lines above the electronic states. [7]

A number of interactions are also presented in the diagram. Absorption and emission processes are depicted as full arrows. Emission is divided into fluorescence and phosphorescence, depending on whether the excited particle has electrons with unpaired spins. Fluorescence is a spin-allowed emission process, where the particle relaxes from a singlet state to the ground state. In singlet states (marked with letter S in the diagram) there are no electrons with unpaired spins, and thus the relaxation is spin-allowed. The particle typically spends 10^{-8} seconds on an excited singlet state before emission. [7]

Phosphorescence is a spin-forbidden process instead. Triplet states (marked with letter T in the diagram) have one set of electrons with unpaired spins. Thus, the transition from a triplet state to the ground state is spin-forbidden, and the particle typically spends 10^{-3} to 10^{0} seconds on a triplet state before relaxation. [7] Therefore it is clear, that phosphorescence is a process with much longer lifetimes than fluorescence.

Nonradiative processes are marked with dashed arrows. They include vibrational relaxations, intersystem crossing and internal and external conversions. In these processes, no emission or absorption of photons is involved.

Vibrational relaxations occur quickly after excitation, when the chromophore relaxes to the lowest vibrational state related to the current electronic state. Vibrational relaxations cause a portion of the absorbed energy to be released as heat. [7, 27]

External conversion refers to an event where the excited particle collides with another particle an relaxes by the collision. On the other hand, internal conversion is a process, where the particle moves from one excited state to another state with the same energy. Internal conversions require vibrational levels of different electronic states to be overlapping. Intersystem crossing is a similar process, where an excited singlet states relaxes to a triplet state with equal energy. [27]

Vibrational relaxations cause a portion of the absorbed energy to dissipate before emission. Thus, the photons emitted by the chromophore have lower energies than the absorbed ones. The wavelength and energy of a photon are connected by equation

$$E = h\frac{c}{\lambda}, \tag{3.2}$$

where λ is the wavelength of the photon and c is the speed of light. Therefore, fluorescence occurs at higher wavelengths in comparison to absorption. This phenomenon is known as Stokes shift. [7, 27]

Photoluminescence is a cyclical process, meaning that a single chromophore can be excited multiple times after relaxing back to the ground state. However, continuous excitation with high intensities can irreversibly destroy a chromophore causing it to lose it's fluorescent properties. Such phenomenon is referred to as photobleaching. [7]

3.2 Fluorescent Materials

A fluorescent material is any material capable of absorbing photons and re-emitting photons whose wavelengths are on the visible spectrum. [7] Fluorescent materials are often referred as chromophores. Two categories of chromophores typically used in research are organic dye molecules and semiconductor quantum dots (QDs). Both are covered in this subsection.

Organic dye molecules or simply fluorophores typically contain either several aromatic groups or numerous π-bonds, which explains their capability of absorbing and emitting photons [7]. Controlled synthesis methods of dyes allow them to be inserted in close proximity of any desired nanostructure. Absorption and emission bands of dyes are often located in the visible spectrum and they possess high quantum yield. However, dyes frequently suffer from low optical stability, short lifetimes of the excited states and narrow absorption bands. [27]

Quantum dots are semiconductor based nanocrystals capable of fluorescence. QDs display similar behaviour as a quantum mechanical particle in a box, that can only have given discrete energy levels. The size of the dot determines the energy levels of the excited states. Thus, the emission and absorption bands are tunable by changing the dot size. Typical QDs are coated with high-band gap materials to increase charge carrier confinement. Typical materials utilized in fabrication of QDs include CdSe, CdTe and ZnS. [7]

Advantages of QDs include high quantum yield, easy tunability of emission wavelengths by altering dot size, high optical stability and long lifetimes of the excited states. QDs have broad absorption and narrow emission spectra. Their main weaknesses are exhibited aggregation and surface defects, that decrease the quality of dots and can induce blinking. Nonradiative Auger recombination can cause energy transfer to another particle in the vicinity of the QD instead of emission. This derogates quantum yield and shortens the lifetimes of excited states. [27]

Both dyes and QDs can be easily synthesized industrially. There are several companies selling both kinds of chromophores for research purposes.

3.3 Fluorescence Spectroscopy

Fluorescence spectroscopy refers to different methods used to acquire information of radiative and nonradiative processes, which excited chromophores are undergoing. Methods of fluorescence spectroscopy can be divided under two categories: steady-state and time-resolved spectroscopy. These approaches are covered in subsections 3.3.1 and 3.3.2.

3.3.1 Steady-State Photoluminescence Spectroscopy

Steady-state spectroscopy measurements are performed by pumping a chromophore using continuous illumination. The chromophore can be dispersed in either a solution or a solid host medium. The pump laser operating on the chromophore's absorption spectrum creates population inversion in the system. That is to say, that more chromophores are on the excited states than on the ground state, resulting in continuous emission signal from the chromophore. The emission spectrum of the chromophore can then be monitored with an appropriate spectrometer. [7, 27]

Since steady-state measurements only reveal the magnitude of emission, it cannot be used to observe nonradioactive processes [7, 27]. However, energy transfer processes can be studied by steady-state measurements comparing emission intensities in the presence and in the absence of energy transfer.

3.3.2 Time-Resolved Photoluminescence Spectroscopy

Time-resolved spectroscopy techniques can be used to acquire additional information that cannot be achieved with steady-state measurements. If a sample contains several chromophores with overlapping emission spectra, it is difficult to distinguish information related to a specific chromophore. Time-resolved data is more efficient while measuring samples of this sort. The described measurements also provide information about chromophore decay times. [7]

Chromophore decay times or lifetimes are an important concept when discussing time-resolved spectroscopy. If a sample is excited by a single laser pulse at time t_0, the excitation will generate an initial population n_0 of excited chromophores. After t_0 the excited chromophores start to relax via both radiative and nonradiative pathways. Relaxation is a random process, resulting in an exponential decay of the excited population given by

$$n(t) = n_0 e^{-t/\tau}, \tag{3.3}$$

where τ is the lifetime of the chromophore. Since relaxations take place both radiatively and nonradiatively, the lifetime is the inverse of the total decay rate $\tau = (k_r + k_{nr})^{-1}$. Lifetime also determines the average time an excited particle remains in the excited state. Lifetime is a characteristic property of each chromophore. [7]

As the amount of excited chromophores decreases after t_0, the emission intensity I decreases as well . Therefore, intensity also follows an exponential decay given by

$$I(t) = I_0 e^{-t/\tau_i}, \tag{3.4}$$

where I_0 is the fluorescence intensity at t_0. [7]

For an excited chromophore with multiple lifetimes the fluorescence intensity is given by

$$\sum_{i=1}^{n} \alpha_i e^{-t/\tau_i}, \tag{3.5}$$

where τ_i are the lifetimes and α_i are the intensities of the lifetime components at t_0, respectively. [7]

Time-domain or pulse fluorometry is the most popular experimental method for time-resolved fluorescence spectroscopy. Frequency-domain method is another popular approach. [27] In time-domain fluorometry the sample is excited by a sharp laser pulse, and the intensity of fluorescence is measured as a function of time. Notably, the excitation pulse needs to be considerably shorter than the measured lifetimes. Most setups use detected photon counts as a unit for intensity. Time-correlated single-photon counting (TCSPC) is a widespread method for acquiring intensity data. Chromophore lifetimes can then be extracted from intensity decay data by fitting the data to assumed decay models. Non-linear least squares method is the most widely used method to achieve this. [7, 27]

If the data consists of a single exponential decay, the interpretation is quite simple. In such case, the lifetime is simply the time from t_0 until intensity has decayed to 1/e of the original value I_0. The lifetime can also be acquired from the slope of intensity versus time when the intensity is plotted on a logarithmic scale. [27] However, circumstances are often more complicated. Even a sample with just two different chromophores can show multiple different decay times. One of the chromophores may act as a quencher, shortening the lifetime of the other dye. Nonetheless, there will also be some chromophores whose lifetimes are not shortened. In this case, three different lifetime components would be observed: the lifetime of the quencher (acceptor) and both quenched and unquenched lifetimes of the other chromophore (donor).

Clearly, the interpretation of time-resolved data is a complicated task. However, an incorrect fit can be distinguished from a correct fit by observing the deviations between measured data and fitted points. A correctly fitted model can be recognised by random deviations centralized on the model. This implies the only source of error being random noise in the data, and thus the fitted model is correct. [7]

3.3.3 Quantum Yield

Quantum yield (often denoted as Φ) determines the efficiency of fluorescence for any given chromophore. It is defined as the ratio between photons emitted and absorbed by the chromophore.

$$\Phi = \frac{number\ of\ emitted\ photons}{number\ of\ absorbed\ photons} \tag{3.6}$$

Φ can get values between zero and one. For an ideal chromophore, quantum yield would be equal to one. However, some amount of excited states caused by photon absorption are always relaxed by other nonradiative processes. Thus, quantum yield can also be expressed as a ratio between radiative (k_r) and nonradiative (k_{nr}) decay rates.

$$\Phi = \frac{k_r}{k_r + k_{nr}} \tag{3.7}$$

k_r is related to relaxation by emission while k_{nr} is correlated to the sum of nonradiative decay channels. Consequently, quantum yield measures the efficiency of emission compared to nonradiative processes. [7, 27]

3.4 Förster Resonance Energy Transfer

Energy transfer refers to a process taking place between two chromophores, one of which is in the excited state and the other in the ground state. The excited chromophore would normally relax by emitting a photon after some time. However, under certain circumstances the energy of the excited state can be transferred to the chromophore in the ground state. As a result, that chromophore promotes to the excited state and will release the energy via emission after some time. The chromophores taking part in the energy transfer process are referred as a donor-acceptor pair. Donor refers to the chromophore that transfers its energy while on the excited state and acceptor is the chromophore that is excited via energy transfer. [7]

Förster resonance energy transfer (FRET) is a radiationless energy transfer process originally discovered by German scientist Theodor Förster on 1946. FRET is a near-field interaction process resulting from coupling between the oscillating electric dipoles of the donor and the acceptor. It is essential to understand, that FRET is a nonradiative pro-

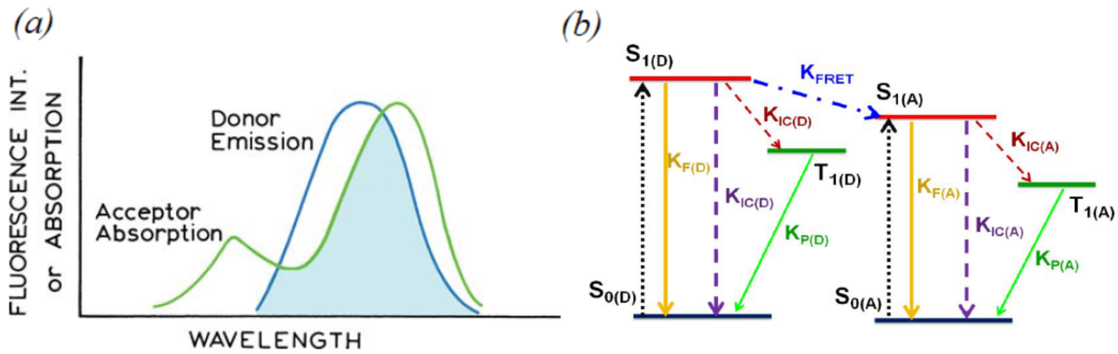

Figure 3.2. *(a) Spectral overlap between donor emission and acceptor absorption highlighted with blue. Such overlap is essential for the occurrence of the FRET process. [7] (b) A Jablonski diagram of a donor (D) and an acceptor (A). Förster resonance energy transfer with the rate of K_{FRET} adds a nonradiative relaxation channel for the acceptor. The rates of fluorescence K_P, phosphorescence K_F, internal conversion K_{IC} and intersystem-crossing K_{ISC} are also visualized for both chromophores. [27]*

cess, where the energy truly is transferred via near-field interactions alone. Emission and re-absorption of photons are not needed to describe this interaction. [7]

During the FRET process, the donor relaxes to the ground state as the energy is transferred to the acceptor, which promotes to one of its excited states. As a result, fluorescence intensity of donors is quenched and intensity of acceptors is enhanced. This is due to several donors participating in the energy transfer process instead of relaxing via photon emission. The number of acceptors in the excited state is also increased, and subsequently acceptor emission is increased. [7] A Jablonski diagram representing FRET between a donor-acceptor pair is shown in Figure 3.2 (b).

Certain requirements need to be fulfilled in order for FRET to occur. The process is extremely sensitive to distance separating the donor-acceptor pair. Typically, a separation distance no larger than 10 nm is required to allow FRET. Growing the separation distance rapidly decreases the efficiency of the process. Furthermore, energy levels of the excited states of both chromophores need to have equal energies in order for the transfer to take place. Therefore, emission spectrum of the donor and absorption spectrum of the acceptor need to overlap. [7] This spectral overlap crucial for FRET is illustrated in Figure 3.2 (a).

3.4.1 Conditions to Obtain the Most Efficient Energy Transfer

Numerous factors affect the efficiency at which FRET takes place between a donor and an acceptor. Altering any of these factors will certainly affect the observed behaviour of the system. As mentioned earlier, separation distance has a crucial role in determining the efficiency. The amount of spectral overlap is another factor greatly affecting the efficiency.

For efficient transfer, the quantum yield of the donor needs to have a large value, since it is the ratio between radiative and nonradiative decay channels. Due to FRET introducing a new nonradiative decay channel to the system, it will compete with other nonradiative processes. If the other nonradiative relaxation channels are negligible (donor has high quantum yield), energy transfer will be more efficient. Additionally, transfer efficiency depends similarly on the absorption coefficient of the acceptor. [7]

Increasing concentration of donors in the system results in increased energy transfer. However, very high concentration of a chromophore will give rise to dimerization, causing the chromophores to react with each other. As a result, dimer molecules will be added to the system, making the resulting fluorescence spectrum extremely hard to interpret. [27] The amount of dye molecules or QDs able to be dissolved in a solvent is also limited. A solution of overly high concentration will have solid aggregated particles dispersed within it, making the sample inhomogeneous.

Lastly, the orientations of donor and acceptor transition dipoles affect the efficiency [7]. Unfortunately, in a typical sample where the chromophores are either dissolved in liquid or a solid host medium, a little can be done to control the orientations.

3.4.2 Energy Transfer Rate

The rate of Förster resonance energy transfer k_{FRET} is given by the following equation

$$k_{FRET} = \frac{1}{\tau_D}(\frac{R_0}{r})^6, \tag{3.8}$$

where τ_D is the lifetime of an unquenched donor, r is the separation distance between donor and acceptor and R_0 is the so-called Förster distance. Förster distance is the value of separation distance where energy transfer efficiency rhas reduced to 50% (Figure 3.3). It is given in Å by

$$R_0 = 0.211(\kappa^2 n^{-4}\Phi_D J(\lambda))^{1/6} \text{ (in Å)}, \tag{3.9}$$

where n is the refractive index of the medium, Φ_D is the quantum yield of the donor in the absence of the acceptor and κ^2 is the orientation factor, which is related to the transition dipoles of donor and acceptor. It can range from 0 to 4, but typically an assumed value of $\kappa^2 = 2/3$ is used in literature, since it describes randomly oriented donors and acceptors. $J(\lambda)$ is the spectral overlap integral used to describe the degree of overlap between donor emission and acceptor absorption spectra. It is given by

$$J(\lambda) = \frac{\int_0^\infty F_D(\lambda)\epsilon_A(\lambda)\lambda^4 d\lambda}{\int_0^\infty F_D(\lambda)d\lambda}, \tag{3.10}$$

where $F_D(\lambda)$ is the fluorescence intensity of the donor in absence of acceptor on wavelength λ. $F_D(\lambda)$ is normalized such that the sum of intensities on all wavelengths gets a value of one. ϵ_A is the extinction coefficient of the acceptor on wavelength λ. [7]

Equations 3.8, 3.9 and 3.10 give a better understanding on the previously discussed factors and their effects on the rate of transferred energy. It is clear that the most important factor on the energy transfer is the separations distance. Indeed, the rate of energy

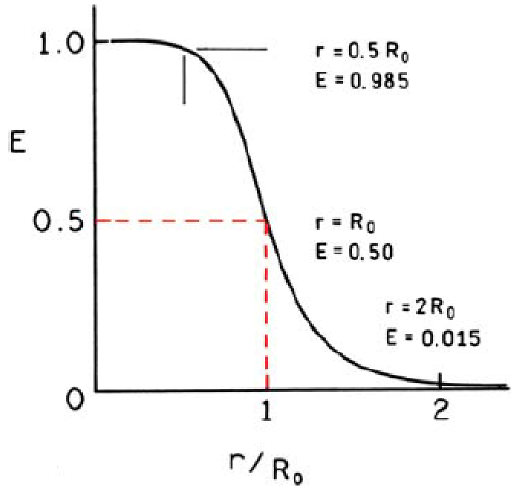

Figure 3.3. *The relation between energy transfer efficiency E and separation distance r. The Förster distance R_0 is the distance where transfer efficiency gets a value of 50 %. As can be seen, a small deviation of distance has a tremendous effect on efficiency. [7]*

transfer depends on the inverse sixth power of distance.

3.4.3 Energy Transfer Efficiency

The efficiency of energy transfer E is defined as the fraction of photons absorbed by the donor that are transferred to the acceptor. It is given by the following equation

$$E_{FRET} = \frac{k_{FRET}(r)}{\tau_D^{-1} + k_{FRET}(r)} \tag{3.11}$$

Substituting equation 3.8 into this yields

$$E_{FRET} = \frac{R_0^6}{R_0^6 + r^6}, \tag{3.12}$$

which again emphasizes the crucial dependence on separation distance. [7] Figure 3.3 displays energy transfer rate as a function of separation distance.

Both steady-state and time-resolved spectroscopy methods can be used to acquire the transfer efficiency. The efficiency can be extracted from measured data using equation

$$E_{FRET} = 1 - \frac{F_{DA}}{F_D} = 1 - \frac{\tau_{DA}}{\tau_D}, \tag{3.13}$$

where F_{DA} is the fluorescence intensity of the donor in the presence of the acceptor, F_D in the absence of the acceptor and τ_{DA} and τ_D are the corresponding lifetimes. [7]

Equation 3.13 is based on the assumption of a donor-acceptor pair with a fixed separation distance. Neither a solution nor a solid host medium containing a mixture of donors and acceptors will fulfill this assumption. Thus, averaging the transfer rate over the assumed spatial distribution of donor–acceptor pairs will be necessary, and the expression for transfer efficiency becomes more complex for such cases. [7]

3.4.4 Applications

Due to the extreme dependence on separation distance, FRET measurements can be used as a spectroscopic ruler. Studying transfer efficiency, distances between sites on proteins and other organic compounds can be acquired. [28]

Another possible application is to utilize energy transfer as a means of compensating absorptive losses in lossy nanostructures. Bringing a fluorescent gain material in a close vicinity of the nanostructure can result in energy being transferred to the structure. [27] However, the short distance where energy transfer remains functional hinders the feasibility of such applications.

4 METHODS

As a part of this thesis, experimental work was performed to find a suitable donor-acceptor pair to investigate FRET mediated by a multilayer nanostructure. The objective will be to fabricate three multilayer structures and use each structure to separate the donors from the acceptors. The first structure will show elliptical behaviour on wavelengths where donor-acceptor pair has spectral overlap. The second structure will show hyperbolic behaviour on these wavelengths, while the third structure's ENZ region will be located within these wavelengths.

In this chapter, methods for modelling and designing multilayer structures are described. Thereafter, fabrication of multilayer nanostructures are discussed. Moreover, the synthesizing process of spin-coated organic dye molecules is explained. Finally, the experimental setup and methods used to characterize the samples are outlined.

4.1 Theoretically Modelling a Multi-layer Nanostructure

The effective parallel and perpendicular permittivities of multi-layer nanostructures were modelled using equations 2.8 and 2.11. The reflectance and transmittance properties of these structures were calculated using transfer-matrix method (TMM). These theoretical calculations were implemented with the aid of Matlab R2018a, which is a software designed for numerical computing and a programming language. The optical constants of the different used materials were adopted from the following references: gold and silver from [29], aluminium from [30], titanium dioxide (TiO_2) from [31], silicon dioxide (SiO_2) from [32], aluminium oxide (Al_2O_3) from [33] and tantalum pentoxide (Ta_2O_5) from [34].

Additionally, simulations utilizing Finite-difference time-domain (FDTD) method were conducted using a commercial software package (Lumerical FDTD Solutions). Silver layers with three different thicknesses are modelled with optical constants taken from Johnson and Christy [29], while the dielectric function of tantalum pentoxide (Ta_2O_5) layers were modelled using the reported data from reference [35]. In these simulations, the incident field was a Transverse Electromagnetic (TEM) plane wave with electric and magnetic fields in X and Y directions, respectively, while wave propagates in Z direction with a normal incident. The transmitted and reflected signals were collected from the top and bottom of the multilayer nanostructures, respectively.

4.2 Sample Preparation and Fabrication

Fused silica (SiO_2) with the thickness of 1.1 mm was used as a substrate for all fabrications related to this thesis. This substrate was used due to the small refractive index and high transparency. To eliminate any possible polar and non-polar impurities, the substrates were sonicated for 20 minutes in acetone and soaked and rinsed with fresh acetone and IPA solvents afterwards. The substrates were later dried with nitrogen blow. Finally, the oxygen reactive ion etching (RIE) machine was used as the for 10 minutes to remove any probable residues.

Dye molecules were dissolved in PMMA A4 photoresist (950 K molecular weight) from Microchem corp. with a mass percent concentration of 0.01%. To avoid aggregation of the incorporated dyes in PMMA, the prepared samples were sonicated at low temperature for 20 minutes. Moreover, to homogenize the prepared samples, the dye-PMMA samples were stirred for at least 90 seconds using a vortex mixer operating at 3000 rpm. Then the active PMMA layer was spin-coated at 4000 rpm for 40 seconds on cleaned substrate to create a layer with the thickness of approximately 200 nm. To avoid any change in the chemical and optical properties of the incorporated dye molecules in PMMA, the samples were not baked using a hot plate. Instead, the samples were left overnight (at least 16 hours) to evaporate the anisole solvent at room temperature.

In upcoming works the fabrication of multilayer nanostructures will be done on top of spin-coated PMMA dye layers on fused silica substrate. This will be achieved using an electron-beam (E-beam) evaporator at the constant rate of 3 Å/sec and a vacuum pressure of 5.6×10^{-6} mbar to deposit metal and dielectric layers on top of each other, while the operating voltage is kept around 9 kV.

E-beam evaporator is a device used for thin and accurate physical vapor deposition of metal and dielectric layers. The device has several crucibles, which contain different metals and dielectric materials. A high voltage and current controlled tungsten filament is used as an electron gun to bombard the crucible with emitted electrons. As a consequence, the material inside the crucible is evaporated. The vapor particles move with high speed in all directions inside the chamber coating each surface, including the sample. [36]

A quartz crystal is used as a thickness monitor. Material evaporating on the crystal surface changes its mass and subsequently its natural frequency. Monitoring this frequency provides information of the deposition process accurately over each second. Due to the thickness being known at every moment, the rate of deposition is calculated automatically. Therefore, the user is able to change the rate of deposition by changing the feed current of the beam source. [36] Figure 4.1 illustrates a scheme for an e-beam evaporator.

The design of the used E-beam evaporator allows the sample chamber and crucible chamber to be separated. This minimizes the influence of heat caused by the electron gun on the physical properties of the spin-coated PMMA layer. During the entire deposi-

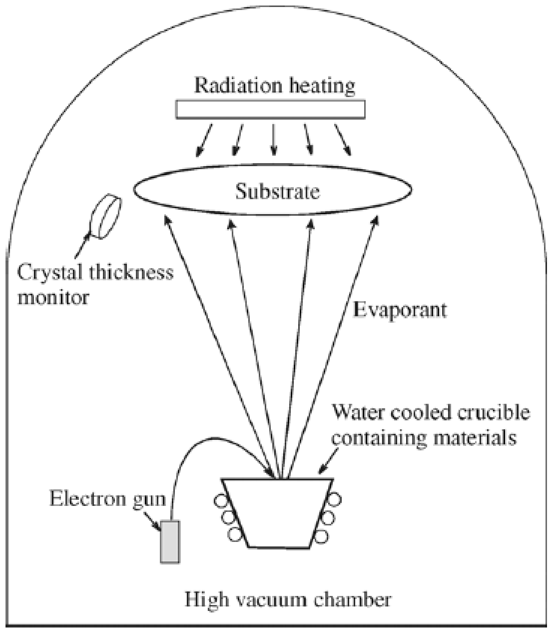

Figure 4.1. *A scheme describing an electron-beam evaporator. [36]*

tion process both chambers of this device are kept under vacuum. Moreover, the sample chamber is cooled down below room temperature with continuous flow of cold water.

4.3 Experimental Setup

Absorbance, photoluminescence and fluorescence lifetime measurements needed for investigating the optical properties of dye molecules were performed on a multi-functional WITec alpha300C confocal Raman microscopy system. The experimental setup utilized in this work is visualized on Figure 4.2.

Two lasers were used to excite the samples. A 375 nm laser was used to excite the samples in the UV range, while a 532 nm laser was used to excite acceptor dye molecules. To generate the 532 nm excitation pulses, the output of a picosecond super-continuum Fianium laser was connected to an acoustic optical tunable filter (AOTF), generating pulses in the visible range (420 nm – 700 nm). PL measurements were performed using continuous wave excitation laser sources, while lifetime measurements were performed utilizing pulsed laser beams. Absorbance results were acquired using a highly bright and stable broadband light source (LDLS EQ-99X).

PL and absorbance spectra of the spin-coated dye samples were acquired utilizing VIS-NIR Flame detector (350 nm-1000 nm) provided by Ocean Insight with integration time of 500 ms. The PL signals were guided to the detector through a 50x Zeiss EC "Epiplan" DIC objective (NA=0.75, WD=1.0 mm). For absorbance measurements a 20x Zeiss EC "Epiplan" DIC objective (NA=0.4, WD=3.0 mm) was used to guide the broadband beam over the samples, while the transmitted signal was collected through a 50x Zeiss LD "Epiplan -Neofluar" (NA=0.55, WD=9.1 mm) objective.

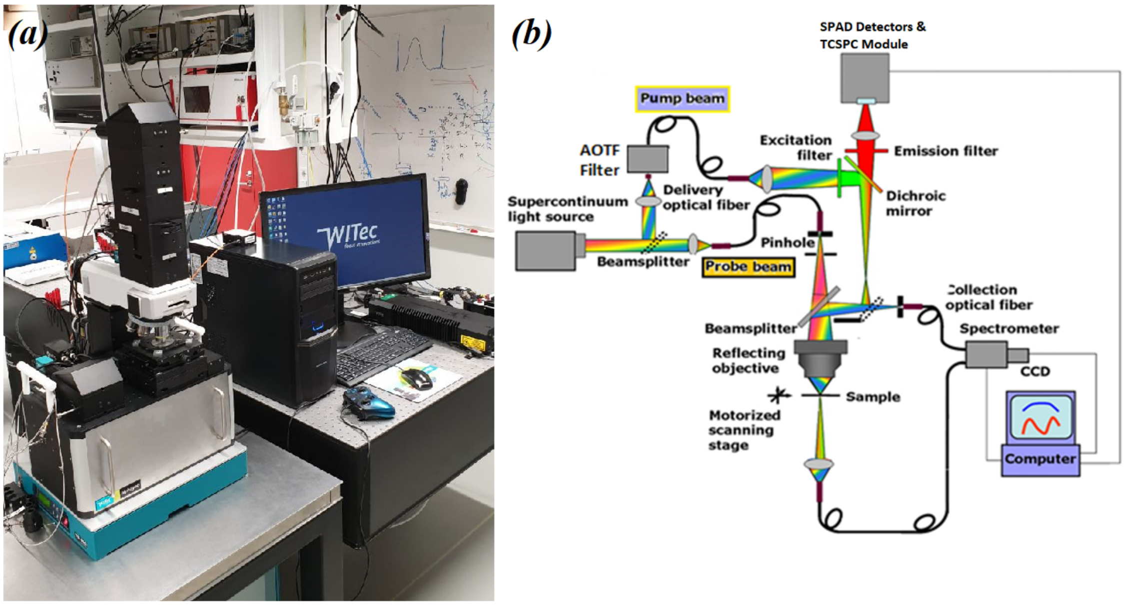

Figure 4.2. *(a) The microscopy setup used to perform all absorbance, photoluminescence and fluorescence lifetime measurements related to this thesis. (b) A scheme describing the microscopy setup.*

The transmittance spectra (Tra) were calculated using the following equation

$$Tra = \frac{I_{Tra} - I_{BG}}{I_{sub} - I_{BG}}, \tag{4.1}$$

where I_{Tra} is the collected transmission spectrum of the samples and I_{sub} stands for the substrate transmission, which was acquired from an uncoated fused silica substrate. The background counts I_{BG} were subtracted from the measured PL and absorbance spectra. The absorbances (Abs) were calculated afterwards by $Abs = -log_{10}(Tra)$ on the acquired transmittance signals. [37]

The reflectance spectra (*Ref*) were calculated utilizing equation

$$Ref = \frac{I_{Ref} - I_{sub}}{I_{source} - I_{BG}}, \tag{4.2}$$

where I_{Ref} is the collected reflection spectrum of the system and I_{Source} is the reference spectrum of the broadband light source, which is measured using a silver coated substrate as a perfect reflector.

For lifetime measurements the photons of the excited sample were collected using the 50x objective and detected by single-photon avalanche diode (SPAD) detectors provided by PicoQuant, which have an extremely high photon detection efficiency up to 70 %. SPADS operate in the range of 400 nm to 1100 nm. The acquired time-correlated single-photon counting data (TCSPC) is processed by a time to digital converter (TDC) module, which is provided by PicoQuant, and the results are analyzed by SymPhoTime 64 software.

5 FRET MEDIATED BY A MULTI-LAYER NANOSTRUCTURE

Experiments by several groups have demonstrated that the hyperbolic regime of a metamaterial can be used to enhance dipole-dipole interactions in general [38, 39] and FRET specifically [8, 10, 38, 39]. In addition to increasing energy transfer rate, the use of HMMs has been shown to allow FRET over distances much longer than usual [8, 38, 39]. However, the underlying mechanisms for these phenomena are still not entirely clear. Furthermore, the influence of an ENZ material on FRET process is still widely unknown.

As a part of this thesis, preparatory work was performed to allow an in-depth study of FRET process mediated by a multi-layer nanostructure. First, several organic dye molecules were characterized to find a suitable donor-acceptor pair needed for the upcoming experiments. After a combination of dye molecules with the desired properties was found, Matlab and FDTD simulations were executed to design three different multi-layer nanostructures, which operate as a hyperbolic metamaterial, an ENZ metamaterial and an elliptical material at the spectral overlap region of the donor-acceptor pair.

5.1 Realizing FRET between a donor-acceptor pair

A suitable donor-acceptor pair needs to fulfill certain criteria. First, the donor needs to have a high quantum yield and the acceptor needs to have high absorptivity, such that pronounced energy transfer can be observed. Second, the donor emission and acceptor absorption spectra must overlap. Finally, the acceptor needs to show a large Stokes shift.

Large Stokes shift is crucial to perform successful lifetime measurements. The photon counting device used to measure lifetimes observes the number of photons hitting the detector, but it cannot measure the photon's energy (wavelength). Thus, any observed photons emitted by the acceptor cause misinterpretation in the measured lifetime of the donor. Therefore, an optical filter is needed to remove acceptor emission from the detection path to obtain precise lifetime data. Using an acceptor with large Stokes shift makes such filtering tremendously easier.

A combination of dye molecules Coumarin 485 (C 485) as the donor and LDS 798 as the acceptor was found to satisfy the mentioned criteria. This was verified by absorbance, PL and lifetime measurements. Thus, this donor-acceptor pair will be used to form the basis of upcoming experiments.

The quantum yield of a chromophore can be measured with an integrating sphere. Due to not having access to such device, examination of literature was used as a means of finding the quantum yields of different possible donors. For the quantum yield of C 485 a value of 0.86 is reported in reference [40].

To measure the absorbance and emission spectra of dye molecules, the molecules were embedded in a solid PMMA as the host medium. This was done by spin-coating a mixture of PMMA A4 (a mixture of 4% PMMA dissolved in 96% of anisole) and dye molecules on top of a fused silica substrate. Previous experiments have shown that a homogeneous and mono-dispersive mixture of PMMA A4 and dye molecules can be achieved, when the weight ratio concentration (wt %) of the prepared dispersion is 0.01%. The weight ratio concentration of a mixture is given by equation

$$wt\% = \frac{m_{\text{dye}}}{m_{\text{PMMA A4}} + m_{\text{dye}}} \approx \frac{m_{\text{dye}}}{m_{\text{PMMA A4}}} = 0.01\% = 0.0001, \tag{5.1}$$

where m_{dye} is the mass of the dye and $m_{\text{PMMA A4}}$ is the mass of PMMA A4 solution. Based on this equation, a mixing ratio of $m_{\text{dye}} = 0.0001 \cdot m_{\text{PMMA A4}}$ was used. A sensitive analytical balance was utilized to measure the masses before mixing.

To ensure that both mixtures had equal amount of dye molecules, a solution of LDS 798 with wt % = 0.01% was made first. The amount of dye molecules n_{dye} in a mixture can be extracted from equation

$$n_{\text{dye}} = \frac{m_{\text{dye}}}{M_{\text{dye}}}, \tag{5.2}$$

where m_{dye} is the mass of dye molecules in the dispersion and M_{dye} is the molar mass of the dye. The molar masses of C 485 and LDS 798 are $M_{\text{C 485}} = 257.21$ g/mol and $M_{\text{LDS 798}} = 428.9$ g/mol, respectively. Using equation 5.2, the number of LDS 798 molecules in the solution was calculated. Then the mass of that many C 485 molecules was acquired using the same equation. This calculated mass was used to prepare the dispersion of C 485 dye molecules in PMMA A4, while the mass of PMMA A4 was considered equal in both LDS 798 and C 485 mixtures. As a result, the number of dye molecules was kept the same in both solutions, resulting in slightly different concentrations.

The absorption and emission spectra of C 485 and LDS 798 are represented in Figure 5.1 (a) and (b), respectively. Figure 5.1 (c) visualizes the spectral overlap between C 485 emission and LDS 798 absorption spectra. Each emission and absorbance value is normalized to unity. The spectral overlap is located at wavelength range of 420 nm to 570 nm.

To realize FRET between this pair, emission and lifetime measurements were performed for donors and acceptors independently, and for a sample in which donors and acceptors were mixed together. The measurements were carried out for three sets of samples. Each set consisted of three spin-coated samples. One sample had C 485 molecules, another one LDS 798 molecules and the last one a mixture of both dyes in PMMA.

For each set of samples, different concentrations of both dyes were used. The solutions

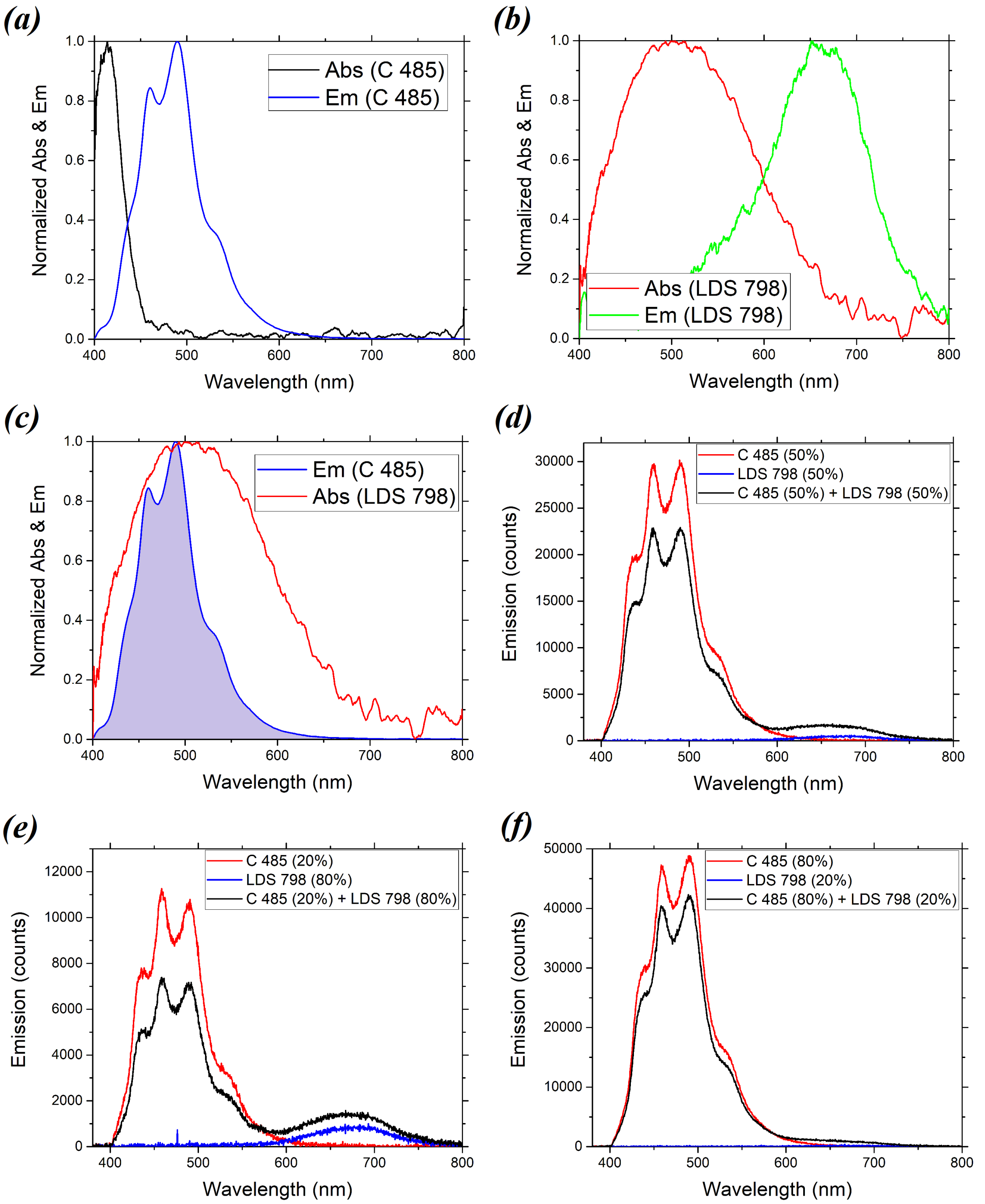

Figure 5.1. *Normalized absorbance and emission spectra of (a) Coumarin 485 and (b) LDS 798. (c) Spectral overlap between the chosen donor and acceptor dye molecules, highlighted in light purple. (d) Emission of bare C 485 and LDS 798 dyes embedded in PMMA and their mixture with different ratios of 50% / 50%, (e) 20% / 80% and (f) 80% / 20%. The reported percentages are the portions of particular dye molecules out of the total number of dye molecules in the sample. The quenching of C 485 emission and enhancement of LDS 798 emission in the mixed sample implies energy transfer between the dye molecules. Modifying donor and acceptor concentrations affects the rate of energy transfer. Each sample was excited with a continuous wave 375 nm laser with equal excitation intensities.*

of wt % = 0.01% described above were used as the base solutions to prepare further solutions with different concentrations. The first set of samples was prepared using solutions that were diluted to contain 50% the amount of dye molecules of the original solutions. The seconds set had C 485 diluted to 20% and LDS 798 to 80% of the original concentration. The final set of samples had C 485 diluted to 80% and LDS 798 to 20%. The diluted solutions were prepared by mixing the original solutions with appropriate amount of PMMA A4. The mixed solutions were made by mixing the original C 485 and LDS 798 solutions with appropriate mixing ratios (20% / 80%, 50% / 50% and 80% / 20%).

The acquired emission results for each set of samples are presented in Figure 5.1 (d), (e) and (f), respectively. It is worth noting that each sample was excited with 375 nm laser at the same intensity. In addition, the number of C 485 molecules is the same in the C 485 sample and the mixed sample. Likewise, the LDS 798 sample and the mixed sample contain an equal number of LDS 798 molecules.

It is clearly seen that the the emission of C 485 is quenched in the sample of mixed donors and acceptors. Additionally, the emission from LDS 798 is enhanced in this sample. Furthermore, enhancement is the weakest when the concentration of LDS 798 is 80% and the strongest when the concentrations is 20%. Similarly, when the concentration of C 485 is 80%, quenching is the weakest. This is in line with the expected results, implying FRET taking place between C 485 and LDS 798.

Fluorescent lifetime measurements were also performed on the described sets of samples to observe the changes in donor lifetime in the presence and absence of the acceptor. The samples were excited with a pulsed 375 nm laser, and a band-pass filter with central wavelength at 450nm and bandwidth of 10nm was placed on the detection path to ensure that only photons emitted by the donor were detected.

The amplitudes and lifetime components were acquired by fitting the intensity decay data to equation 3.5. These results are visualized in table 5.1. The decrease in donor lifetime is evident from the results. The lifetimes of samples consisting of only C 485 show a single lifetime component around 4.7 ns. Slight deviations of lifetime from sample to sample are explained by noise in the measured decay signal and slight uncertainties in fitting.

When C 485 is coupled with LDS 798, two lifetime components become apparent. The longer component is greater than 4 ns and it represents the lifetime of uncoupled donor molecules. On the other hand, the lifetime component ranging from 2.19 ns to 2.72 ns corresponds to the shortened lifetime of donors coupled with acceptors. These donors are participating in the FRET process.

The concentrations of donors and acceptors are different in each mixed sample, resulting in different lifetime and amplitude components. The sample where the concentration of donors is less than that of the acceptors will be discussed to interpret these results. When compared to the other samples, two features are striking. First, the lifetime of the shortened component is quenched in this sample more than the other samples. Second, the corresponding amplitude is larger.

Table 5.1. *Coumarin 485 lifetimes in the presence and in the absence of LDS 798.*

Sample	Amplitudes	Lifetime components	Average lifetime
C 485(20%)	-	4.66 ns	4.66 ns
C 485(50%)	-	4.66 ns	4.66 ns
C 485(80%)	-	4.75 ns	4.75 ns
C485(20%) + LDS798(80%)	A_1: 9.0 A_2: 15.8	τ_1: 4.20 ns τ_2: 2.19 ns	3.73 ns
C485(50%) + LDS798(50%)	A_1: 9.0 A_2: 5.0	τ_1: 4.46 ns τ_2: 2.42 ns	3.98 ns
C485(80%) + LDS798(20%)	A_1: 10.0 A_2: 4.1	τ_1: 4.70 ns τ_2: 2.72 ns	4.31 ns

The quenching magnitude of the short lifetime component is correlated to the strength of resonance energy transfer. Stronger shortening of lifetime implies that more pronounced coupling takes place between the molecules. The amplitudes of the short and long lifetime components are related to the amount of coupled and uncoupled donor molecules, respectively. A large amplitude related to the shortened component signifies that most donors are participating in FRET. When there are excess acceptors and a shortage of donors, most of the donors are coupled with the acceptors. Additionally, the coupling is more pronounced in such case. In turn, when there are excess donors, many donors remain uncoupled. Consequently, these donors show the usual unquenched lifetime and the average lifetime of the hybrid system remains close to that of the bare donors. These observations are a clear evidence of FRET process occurring between the chosen dye molecules.

Based on the combined emission and lifetimes results, Coumarin 485 and LDS 798 seem ideal candidates for the donor-acceptor pair. Since their spectral overlap lies within wavelengths from 420 nm to 570 nm, the multi-layer structures were designed based on this overlap.

5.2 Design of Multi-layer Nanostructures

To study mediated FRET over structures with different optical properties, three distinct multi-layer nanostructures have to be designed. Since energy transfer takes place between 420 nm to 570 nm, these wavelengths are the point of interest for this study, in which three different structures will be presented. One structure will have an elliptical isofrequency surface on these wavelengths. Another structure will behave as an ENZ material on these wavelengths and the final structure will display hyperbolic dispersion.

The desired behaviour of a multi-layer structure is achieved by manipulating the ENZ wavelengths. The first sample should show elliptical behaviour from 420 nm to 570 nm. On wavelengths lower than the ENZ point, both permittivity components have a positive

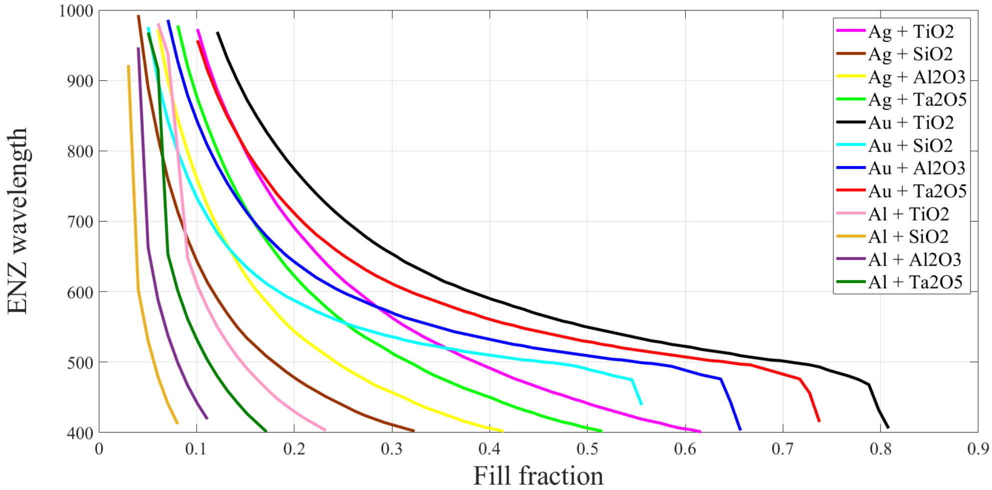

Figure 5.2. *ENZ-wavelengths versus fill fraction calculated for different combinations of metals and dielectrics*

value. Thus, the ENZ point has to be located on higher wavelengths than the overlap to achieve elliptical behaviour in the spectral region of interest. In this study, the ENZ-wavelength of elliptical sample will be 650 nm.

On the other hand, the ENZ sample will have its ENZ point on the spectral overlap region. In this study, the ENZ wavelength of the ENZ sample will be 520 nm.

Finally, wavelengths higher than the ENZ wavelength demonstrate hyperbolic dispersion due to the effective permittivity components having different signs. Thus, the hyperbolic structure will need to have its ENZ wavelengths lower than the overlap. In this study, the ENZ wavelength of hyperbolic sample will be 420 nm.

To prevent any additional factors altering the energy transfer rate, each structure will be fabricated using same metal and dielectric. Furthermore, the total thickness of each structure must be equal. The ENZ wavelengths will be controlled via layer thicknesses. However, there are some practical limitations on the thicknesses. Layers thinner than 10 nm often do not form uniform and homogeneous surfaces, consequently weakening the sample quality. Layers thicker than 40 nm do not fulfill the criteria of being much smaller than the wavelengths of visible light. Preferably, the metal thickness should be kept as thin as possible to minimize losses in the structure.

The structures need to be designed such that the layer thicknesses only get values between 10 and 40 nm. Fill fraction, as defined in equation 2.4 is the ratio of metal thickness to overall thickness. As long as fill fraction gets values between 0.2 and 0.8, both layer thicknesses can stay within 10 and 40 nm simultaneously. Thus, the ideal combination of a metal and a dielectric will allow ENZ wavelengths at 420 nm, 520 nm and 650 nm, accompanied by fill fraction values between 0.2 and 0.8. To examine combinations of available materials, a plot of ENZ wavelength versus fill fraction was calculated for several combinations of materials based on equation 2.8. Results are visualized in Figure

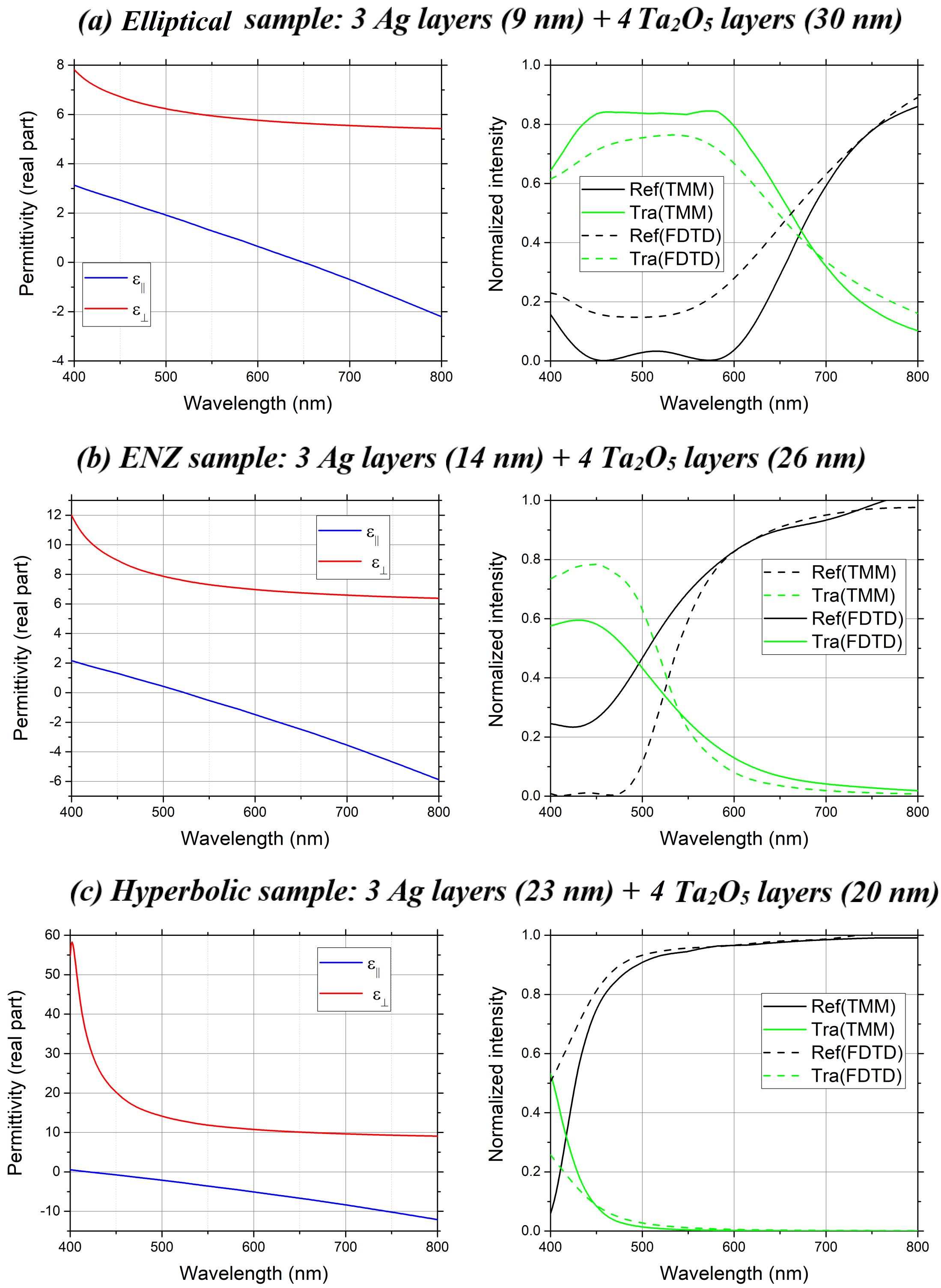

Figure 5.3. *Calculated permittivity components (blue and red), reflectances (black) and transmittances (green) of the designed multi-layer structures. TMM calculations are shown as solid lines and FDTD simulations as dashed lines. (a) The parallel permittivity components of the samples pass through zero at (a) 650 nm for the elliptical, (b) 520 nm for the ENZ and (c) 420 nm for the hyperbolic sample.*

5.2. A combination of silver (Ag) and tantalum pentoxide (Ta_2O_5) strikes as the ideal candidate.

As Ag accompanied by Ta_2O_5 was found to be an appropriate combination, it was used for the designs. Three layers of metal and four layers of dielectric were used to model the permittivities of a multi-layer structure using equation 2.8. Suitable designs were found for each three wavelengths, and the calculated permittivities of each design are presented in Figure 5.3. An ENZ point at 420 nm can be achieved with four 20 nm thick layers of Ta_2O_5 and three 23 nm thick layers of Ag. An ENZ point at 520 nm can be achieved with four 26 nm thick layers of Ta_2O_5 and three 14 nm thick layers of Ag. ENZ point at 650 nm can be achieved with four 30 nm thick layers of Ta_2O_5 and three 9 nm thick layers of Ag.

Reflectance and transmittance values for each structure were calculated utilizing both TMM and FDTD methods. The acquired results are displayed in Figure 5.3. Since the effective optical constants of a multi-layer structure cannot be directly measured, the characterization of fabricated metamaterials will be done by measuring the transmittance and reflectance of each structure. Therefore, the quality of a fabricated sample is evaluated by observing if the measured transmittance and reflectance match with the simulated values. The optical constants can be extracted from measured reflectance and transmittance utilizing inverse TMM approach.

5.3 Results and Discussion

FRET taking place between C 485 and LDS 798 dye molecules was demonstrated utilizing steady-state and time-resolved spectroscopy measurements. Three different multilayer nanostructures were designed to behave differently in the overlap region of donor emission and acceptor absorption spectra.

To perform the measurements in practice, the dye molecules will be separated by depositing the donors on the bottom and the acceptors on top of the multi-layer structures. To avoid direct coupling between the dye molecules and the plasmon oscillations of silver, the top and bottom layers are considered as dielectric layers. Thus, the final designs are made of four dielectric and three metal layers. As FRET is a distance sensitive process, minor adjustments were done so that the total thickness of each proposed structure would be 147 nm. The designs are presented in Figure 5.4.

The elliptical sample is expected to not display any extraordinary behaviour. For this reason, it could be regarded as a control sample. Both effective permittivity components will have a positive sign on the wavelengths of energy transfer. Thus, the optical properties of the structure are expected to match those of a conventional dielectric. Since FRET is normally achievable only when the separation distance is much less than the total thickness of the structure, no signature of energy transfer is expected to be observed on this sample.

The hyperbolic sample is expected to mediate FRET even though the thickness of the

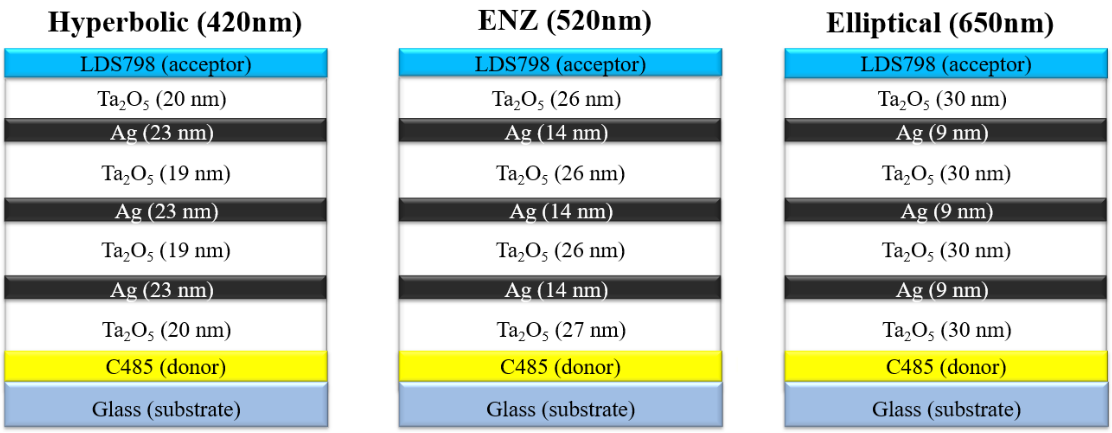

Figure 5.4. *The proposed final multilayer structures consist of alternating layers of silver and tantalum pentoxide. Coumarin 485 acts as the donor and LDS 798 as the acceptor. The ENZ wavelength of each structure is represented within parentheses.*

structure would normally prevent the transfer. Similar results have been previously reported in [38, 39]. However, the exact mechanisms behind this phenomenon remain unexplored. Some sources claim that the effect is explained by the increased PDOS [8], while others argue that the transfer efficiency is not correlated with the PDOS [10].

FRET mediated by an ENZ metamaterial is the most novel concept of this study. Previous studies on this matter are sparse, although there have been some reports that efficient FRET can be achieved using an ENZ medium [8, 41]. Since FRET is caused by interactions between electric dipoles, it is limited to the optical near-field of the molecules, only spanning to subwavelength distances. As discussed in section 2.4, an ENZ-material results in waves with high phase velocity, consequently stretching wavelengths inside such material. As the wavelengths are increased, the near-field interactions could be extended over longer distances, consequently allowing FRET to occur like there was no material separating the donors and acceptors at all. Another possible explanation could be related to field enhancement effect related to ENZ metamaterials. Accordingly, effective near-field coupling over farther distances could still be perceived between a donor-acceptor pair.

The underlying mechanisms explaining the influence of multi-layer structures on energy transfer are still widely unknown. Therefore, a logical next step of this research would be to find a sufficient explanation of these mechanisms. Transient absorption spectroscopy could be an interesting method used to reveal the ultrafast dynamics of FRET between a donor-acceptor pair. Furthermore, interpreting these dynamics could clarify the physics behind the behaviour of each structure.

6 CONCLUSION

Hyperbolic metamaterials can be utilized to achieve hyperbolic dispersion, propagating waves with large k-vectors, increased density of photonic states and epsilon-near-zero. Consequently, they have numerous applications in the field of photonics. Two of the most common practical approaches to fabricate such materials are alternating dielectric and metal nanolayers and metal nanorods embedded in a dielectric host medium. In this thesis, multi-layer nanostructures were reviewed as a way to achieve elliptical, epsilon-near-zero and hyperbolic behaviour.

Förster resonance energy transfer is a process occurring between a pair of fluorescent materials. It is a consequence of coupling between two oscillating electric dipoles, and thus is limited to the occurred near-field interaction (maximum separation distance of approximately 10 nm).

The goal of this thesis was to study how the maximum distance and efficiency of FRET can be increased, when the donors and acceptors are separated by a multi-layer nanostructure. Steady-state and time-resolved PL spectroscopy methods were utilized to realize energy transfer between a donor-acceptor pair of two organic dye molecules, Coumarin 485 and LDS 798. Observed quenching of donor emission intensity and lifetime along with increased acceptor emission are clear evidence of energy transfer between the pair.

The effective permittivities, transmittances, and reflectances of multi-layer nanostructures were modelled utilizing effective medium theory calculations along with transfer matrix and finite-difference time-domain methods. Multi-layer nanostructures consisting of silver (Ag) and tantalum pentoxide (Ta_2O_5) were shown to allow the fabrication of nanostructures with ENZ-wavelengths at 420 nm, 520 nm and 650 nm. Thus, this combination is the ideal choice to study the effects of elliptical, ENZ, and hyperbolic regimes of a multi-layer nanostructure on the FRET process between C 485 and LDS 798.

The next step of this research should be to fabricate the designed nanostructures and observe energy transfer in the presence of each structure. Transient absorption spectroscopy measurements could be an approach to correctly explain the so far unknown mechanisms behind the mediated FRET.

REFERENCES

[1] Pendry, J. B. Negative refraction makes a perfect lens. *Physical review letters* 85.18 (2000), 3966.

[2] Guo, Y., Newman, W., Cortes, C. L. and Jacob, Z. Applications of hyperbolic metamaterial substrates. *Advances in OptoElectronics* 2012 (2012).

[3] Shekhar, P., Atkinson, J. and Jacob, Z. Hyperbolic metamaterials: fundamentals and applications. *Nano convergence* 1.1 (2014), 14.

[4] Alu, A., Silveirinha, M. G., Salandrino, A. and Engheta, N. Epsilon-near-zero metamaterials and electromagnetic sources: Tailoring the radiation phase pattern. *Physical review B* 75.15 (2007), 155410.

[5] Mahmoud, A. M. and Engheta, N. Wave–matter interactions in epsilon-and-mu-near-zero structures. *Nature communications* 5.1 (2014), 1–7.

[6] Jacob, Z., Kim, J.-Y., Naik, G. V., Boltasseva, A., Narimanov, E. E. and Shalaev, V. M. Engineering photonic density of states using metamaterials. *Applied physics B* 100.1 (2010), 215–218.

[7] Lakowicz, J. R. *Principles of fluorescence spectroscopy*. Springer Science & Business Media, 2013.

[8] Deshmukh, R., Biehs, S.-A., Khwaja, E., Galfsky, T., Agarwal, G. S. and Menon, V. M. Long-range resonant energy transfer using optical topological transitions in metamaterials. *ACS Photonics* 5.7 (2018), 2737–2741.

[9] Biehs, S.-A. and Agarwal, G. Qubit entanglement across ε-near-zero media. *Physical Review A* 96.2 (2017), 022308.

[10] Roth, D. J., Nasir, M. E., Ginzburg, P., Wang, P., Le Marois, A., Suhling, K., Richards, D. and Zayats, A. V. Förster Resonance Energy Transfer inside Hyperbolic Metamaterials. *ACS Photonics* 5.11 (2018), 4594–4603.

[11] Poddubny, A., Iorsh, I., Belov, P. and Kivshar, Y. Hyperbolic metamaterials. *Nature photonics* 7.12 (2013), 948.

[12] Hecht, E. *Optics*. eng. Fifth edition. Harlow, Essex, England: Pearson Education, 2017. ISBN: 978-1-292-09693-3.

[13] Cortes, C., Newman, W., Molesky, S. and Jacob, Z. Quantum nanophotonics using hyperbolic metamaterials. *Journal of Optics* 14.6 (2012), 063001.

[14] Nikolaev, I. S., Vos, W. L. and Koenderink, A. F. Accurate calculation of the local density of optical states in inverse-opal photonic crystals. *JOSA B* 26.5 (2009), 987–997.

[15] Novotny, L. and Hecht, B. *Principles of nano-optics*. Cambridge university press, 2012.

[16] Rashed, A. R., Yildiz, B. C., Ayyagari, S. R. and Caglayan, H. Hot electron dynamics in ultrafast multilayer epsilon-near-zero metamaterials. *Physical Review B* 101.16 (2020), 165301.

[17] Kieliszczyk, M., Janaszek, B., Tyszka-Zawadzka, A. and Szczepanski, P. Tunable spectral and spatial filters for the mid-infrared based on hyperbolic metamaterials. *Applied optics* 57.5 (2018), 1182–1187.

[18] Krishnamoorthy, H. N., Jacob, Z., Narimanov, E., Kretzschmar, I. and Menon, V. M. Topological transitions in metamaterials. *Science* 336.6078 (2012), 205–209.

[19] Engheta, N. Pursuing near-zero response. *Science* 340.6130 (2013), 286–287.

[20] Enoch, S., Tayeb, G., Sabouroux, P., Guerin, N. and Vincent, P. A metamaterial for directive emission. *Physical Review Letters* 89.21 (2002), 213902.

[21] Forati, E., Hanson, G. W. and Sievenpiper, D. F. An epsilon-near-zero total-internal-reflection metamaterial antenna. *IEEE Transactions on Antennas and Propagation* 63.5 (2015), 1909–1916.

[22] Torres Landivar, V. Plasmonics and metamaterials at terahertz frequencies. (2014).

[23] Argyropoulos, C., Chen, P.-Y., D'Aguanno, G., Engheta, N. and Alu, A. Boosting optical nonlinearities in ε-near-zero plasmonic channels. *Physical Review B* 85.4 (2012), 045129.

[24] Vesseur, E. J. R., Coenen, T., Caglayan, H., Engheta, N. and Polman, A. Experimental verification of n= 0 structures for visible light. *Physical review letters* 110.1 (2013), 013902.

[25] Javani, M. H. and Stockman, M. I. Real and imaginary properties of epsilon-near-zero materials. *Physical Review Letters* 117.10 (2016), 107404.

[26] Silveirinha, M. and Engheta, N. Tunneling of electromagnetic energy through subwavelength channels and bends using ε-near-zero materials. *Physical review letters* 97.15 (2006), 157403.

[27] Rashed, A. R., Bartolino, R., Versace, C. C. and Strangi, G. Absorpitive losses mitigation in gain-plasmon hybrid systems as optical metamaterials. PhD thesis. 2013.

[28] Stryer, L. Fluorescence energy transfer as a spectroscopic ruler. *Annual review of biochemistry* 47.1 (1978), 819–846.

[29] Johnson, P. B. and Christy, R.-W. Optical constants of the noble metals. *Physical review B* 6.12 (1972), 4370.

[30] Rakić, A. D. Algorithm for the determination of intrinsic optical constants of metal films: application to aluminum. *Applied optics* 34.22 (1995), 4755–4767.

[31] Siefke, T., Kroker, S., Pfeiffer, K., Puffky, O., Dietrich, K., Franta, D., Ohlıdal, I., Szeghalmi, A., Kley, E.-B. and Tünnermann, A. Materials pushing the application limits of wire grid polarizers further into the deep ultraviolet spectral range. *Advanced Optical Materials* 4.11 (2016), 1780–1786.

[32] Malitson, I. H. Interspecimen comparison of the refractive index of fused silica. *Josa* 55.10 (1965), 1205–1209.

[33] Dodge, M. J. Refractive index. *Handbook of laser science and technology* 2 (1986), 30.

[34] Rodrıguez-de Marcos, L. V., Larruquert, J. I., Méndez, J. A. and Aznárez, J. A. Self-consistent optical constants of SiO 2 and Ta 2 O 5 films. *Optical Materials Express* 6.11 (2016), 3622–3637.

[35] Rodriguez-de Marcos, L. V., Larruquert, J. I., Mendez, J. A. and Aznarez, J. A. Self-consistent optical constants of SiO 2 and Ta 2 O 5 films. *Optical Materials Express* 6.11 (2016), 3622–3637.

[36] Xu, N. and Huq, S. E. Novel cold cathode materials and applications. *Materials Science and Engineering: R: Reports* 48.2-5 (2005), 47–189.

[37] McNaught, A. D., Wilkinson, A. et al. *Compendium of chemical terminology*. Vol. 1669. Blackwell Science Oxford, 1997.

[38] Newman, W. D., Cortes, C. L., Afshar, A., Cadien, K., Meldrum, A., Fedosejevs, R. and Jacob, Z. Observation of long-range dipole-dipole interactions in hyperbolic metamaterials. *Science advances* 4.10 (2018), eaar5278.

[39] Biehs, S.-A., Menon, V. M. and Agarwal, G. Long-range dipole-dipole interaction and anomalous Förster energy transfer across a hyperbolic metamaterial. *Physical Review B* 93.24 (2016), 245439.

[40] Vijila, C. and Ramalingam, A. Photophysical characteristics of coumarin 485 dye doped poly (methyl methacrylate) modified with various additives. *Journal of Materials Chemistry* 11.3 (2001), 749–755.

[41] Li, Y., Nemilentsau, A. and Argyropoulos, C. Resonance energy transfer and quantum entanglement mediated by epsilon-near-zero and other plasmonic waveguide systems. *Nanoscale* 11.31 (2019), 14635–14647.